Size Effects on Strength, Toughness, and Ductility

By Alberto Carpinteri,[1] Member, ASCE

Abstract: Strain localization for slabs in tension and curvature localization for beams in flexure are associated with the fracture toughness of the material. Even if no initial cracks are supposed to exist in the sturcture, the concepts of fracture mechanics are applicable. Size-scale and slenderness are demonstrated to have a fundamental influence on the global structure behavior, which can range from ductile to brittle when softening is taken into account. Whereas in classical plasticity and damage theory geometrically similar structures exhibit congruent behavior since only energy dissipation per unit volume is allowed, when energy dissipation per unit area is also considered (strain or curvature localization), the global brittleness becomes scale-dependent. A limit analysis for beams in flexure is proposed, taking into account the cohesive forces developing between the two opposite crack surfaces. Such a simple approach shows a clear trend toward brittle behavior and catastrophic events for large size and slenderness. When snap-back instability occurs, the softening load-deflection curve exhibits a positive slope and its path becomes virtual. If the loading process is deflection-controlled, the loading capacity of the beam will exhibit a discontinuity with a negative jump. Such results are confirmed by refined finite element investigation.

Introduction

Several materials used in civil engineering, e.g., concrete, rocks, and fiber-reinforced cement composites, exhibit softening in their ultimate behavior under loading. This means that after the elastic, hardening, and/or plastic stages, the load sustained by the material element begins to decrease if the deformation is further increased (Bažant 1976; Carpinteri 1985a; Hillerborg et al. 1976; Ingraffea and Gerstle 1985; Jenq and Shah 1985; Roelfstra and Wittman 1986; Rots et al. 1987).

Softening behavior is considered unstable only if the loading process is load-controlled. When the loading process is strain-controlled, the material element behaves in a stable manner, and the descending load-deformation law may be experimentally detected.

When softening is involved in the mechanical behavior of a structural component not homogeneous or not homogeneously loaded, it is accompanied by strain-localization. For the uniaxial tensile loading of slabs, the constitutive law from stress-strain becomes stress displacement (Hillerborg et al. 1976), while for the bending of beams, the constitutive law from moment versus curvature becomes moment versus rotation (Bažant 1976; Maier 1968). Equivalently, a stress-strain and a moment-curvature law, respectively valid in a slab band width (Bažant 1984) and in a beam contamination length (Maier 1968), may be utilized for softening.

The objective of the present paper is to relate strain or curvature localization to the fracture toughness of the material. Even if no initial cracks are supposed to exist in the structure, the concepts of fracture mechanics (Car-

[1]Prof. of Struct. Mech., Politecnico di Torino, 10129 Torino, Italy.

Note. Discussion open until December 1, 1989. To extend the closing date one month, a written request must be filed with the ASCE Manager of Journals. The manuscript for this paper was submitted for review and possible publication on December 29, 1987. This paper is part of the *Journal of Engineering Mechanics*, Vol. 115, No. 7, July, 1989. ©ASCE, ISSN 0733-9399/89/0007-1375/$1.00 + $.15 per page. Paper No. 23617.

pinteri 1985b; Carpinteri 1986b; Carpinteri and Fanelli 1987; Jenq and Shah 1985; Petersson 1981). The size-scale and the slenderness of the structure are demonstrated to have a fundamental influence on global structural behavior. Whereas in elasticity and plasticity, geometrically similar structures exhibit the same behavior, when softening is taken into account, the structural behavior ranges from ductile to brittle only by increasing size-scale and/or beam slenderness and keeping material properties and external constraints unchanged. In classical plasticity and damage theory, only energy dissipation per unit of volume is allowed, whereas if energy dissipation per unit area is also considered (i.e., strain or curvature localization), the global brittleness becomes scale-dependent (Dougill 1976; Mazar and Lemaitre 1985).

Uniaxial tensile geometry and three-point bending geometry are herein considered, assuming a linear stress-displacement cohesive law. For both these cases, it is possible to consider a dimensionless brittleness number (Carpinteri 1981a, 1981b, 1982a, 1982b, 1985a, 1985b, 1985c, 1986a, 1986b, 1987; Carpinteri et al. 1986a, 1986b, 1986c, 1987; Carpinteri and Fanelli 1987; Carpinteri and Sih 1984), which is a function of size-scale, beam slenderness, and material properties (including fracture energy G_F. For each structural geometry, there is a lower bound to this number, below which the mechanical behavior is unstable with rapid and uncontrollable crack propagation, even if the loading process is deflection-controlled. It is possible to prove that such brittle behavior is due to snap-back instability (Carpinteri 1985a, 1985b, 1985c, 1986a, 1987; Carpinteri et al. 1986a, 1986b, 1986c, 1987; Carpinteri and Fanelli 1987). In these cases, the softening load-deflection curve exhibits a positive slope, and its path becomes virtual.

Three-Point Bending of Beams

The linear elastic behavior of a three-point bending, initially uncracked beam may be represented by the following dimensionless equation:

$$\tilde{P} = \frac{4}{\lambda^3}\tilde{\delta} \qquad (1)$$

where the dimensionless load and central deflection are respectively given by

$$\tilde{P} = \frac{Pl}{\sigma_u t b^2} \qquad (2)$$

$$\tilde{\delta} = \frac{\delta l}{\epsilon_u b^2} \qquad (3)$$

in which l = beam span; b = beam depth, t = beam thickness, $\lambda = l/b$.

Once the ultimate tensile stress σ_u or strain ϵ_u is achieved at the lower beam edge, a fracturing process in the central cross section is supposed to start. Such a process admits a limit situation as is shown in Fig. 1. The limit stage of the fracturing and deformation process may be considered as that of two rigid parts connected by the hinge A in the upper beam edge. The equilibrium of each part is ensured by the external load, the support reaction, and the closing cohesive forces. The latter depend on the distance between the two interacting surfaces; increasing the distance w, the cohesive forces

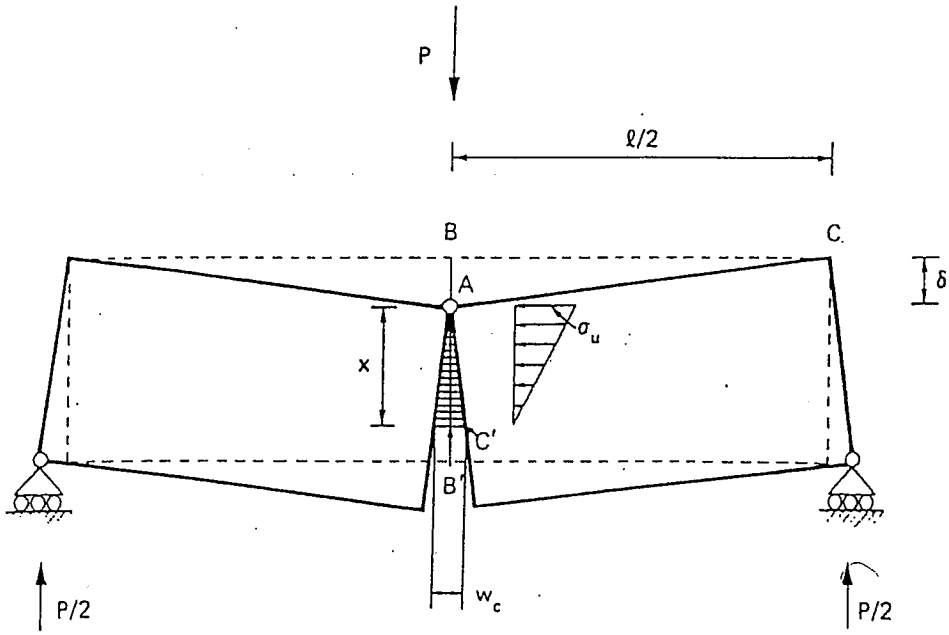

FIG. 1. Limit-Situation of Complete Fracture with Cohesive Forces

decrease linearly till they vanish for $w \geq w_c$.

The geometrical similitude of the triangles ABC and AB′C′ in Fig. 1 provides

$$\frac{\delta}{\frac{l}{2}} = \frac{\frac{w_c}{2}}{x} \quad \ldots\ldots (4)$$

where x = the extension of the triangular distribution of cohesive forces. Eq. 4 can be rearranged as

$$x = \frac{w_c l}{4\delta} \quad \ldots\ldots (5)$$

The rotational equilibrium around point A is possible for each beam part only if the moments of support reaction and cohesive forces, respectively, are equal:

$$\frac{P}{2}\frac{l}{2} = \frac{\sigma_u x t}{2}\frac{x}{3} \quad \ldots\ldots (6)$$

Recalling Eq. 5, the relation between load and deflection may be obtained as

$$P = \frac{\sigma_u t l w_c^2}{24}\frac{1}{\delta^2} \quad \ldots\ldots (7)$$

Eq. 7 can be represented in dimensionless form as follows:

$$\tilde{P} = \frac{1}{6}\left(\frac{s_E \lambda^2}{\epsilon_u \tilde{\delta}}\right)^2 \quad \ldots\ldots (8a)$$

with

$$S_E = \frac{w_c}{2b} = \frac{G_F}{\sigma_u b} \quad \ldots\ldots (8b)$$

in which $G_F = 1/2\ \sigma_u w_c$ = the material fracture energy.

While the linear Eq. 1 describes the elastic behavior of the beam, initially uncracked, the hyperbolic Eq. 8 represents the asymptotical behavior of the same beam, totally cracked. Eq. 1 is valid only for load values lower than that producing the ultimate tensile strength σ_u at the lower beam edge:

$$\tilde{P} \leq \frac{2}{3} \quad \ldots\ldots (9)$$

On the other hand, Eq. 8 is valid only for deflection values higher than that producing a cohesive zone of extension x equal to the beam depth b:

$$x \leq b \quad \ldots\ldots (10)$$

From Eqs. 5 and 10, it follows that

$$\tilde{\delta} \geq \frac{s_E \lambda^2}{2\epsilon_u} \quad \ldots\ldots (11)$$

The bounds of Eqs. 9 and 11, upper for load and lower for deflection, respectively, can be transformed into two equivalent bounds, both upper for deflection and load. Eqs. (1) and (9) provide

$$\tilde{\delta} \leq \frac{\lambda^3}{6} \quad \ldots\ldots (12)$$

whereas Eqs. (8) and (11) provide

$$\tilde{P} \leq \frac{2}{3} \quad \ldots\ldots (13)$$

Conditions represented by Eqs. 9 and 13 are coincident. Therefore, a stability criterion for elastic-softening beams may be obtained comparing Eqs. 11 and 12. When the two domains are separated, it may be presumed that the two $P = \delta$ branches, linear and hyperbolic, are connected by a regular curve [Fig. 2(*a*)]. On the other hand, when the two domains are partially overlapped, it is well-founded to consider them as connected by a curve with a highly negative or even positive slope [Fig. 2(*b*)].

Unstable behavior and catastrophic events (snap-back) are then expected for

$$\frac{s_E \lambda^2}{2\epsilon_u} \leq \frac{\lambda^3}{6} \quad \ldots\ldots (14)$$

and the brittleness condition for the three-point bending geometry becomes

$$\frac{s_E}{\epsilon_u \lambda} \leq \frac{1}{3} \quad \ldots\ldots (15)$$

The system is brittle for low brittleness numbers s_E, high ultimate strains

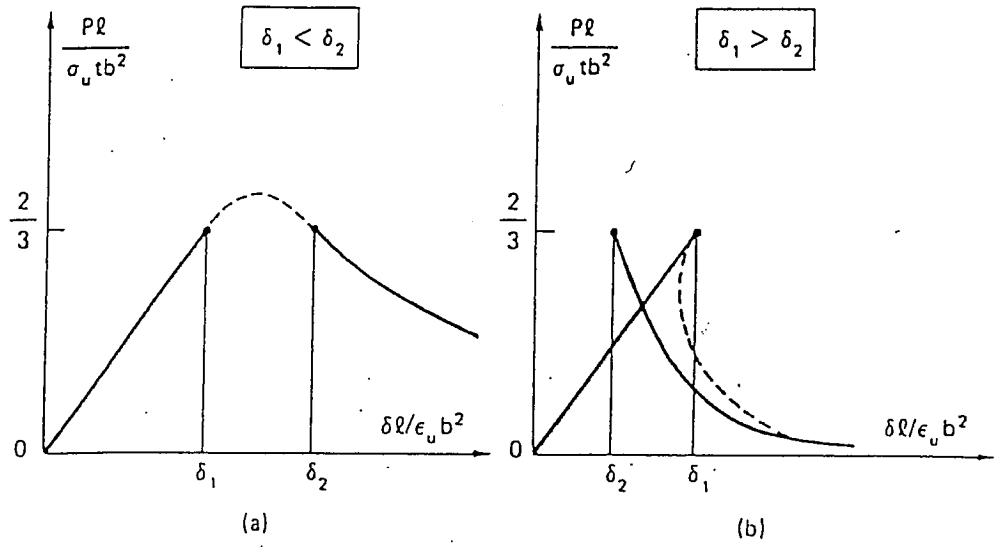

FIG. 2. Load-Deflection Diagrams: (*a*) Ductile; (*b*) Brittle Condition ($\delta_1 = \lambda^3/6$; $\delta_2 = s_E\lambda^2/2\ \epsilon_u$)

ϵ_u, and large slendernesses λ. Observe that the same dimensionless ratio $s_E/\epsilon_u\lambda$ appears also in the case of uniaxial tension geometry, where the upper bound for brittleness is equal to 1/2 (Carpinteri 1986b).

The global brittleness of the beam can be defined as the ratio of the ultimate elastic energy contained in the body to the energy dissipated by fracture:

$$\text{Brittleness} = \frac{\frac{1}{2}P_u\delta_u}{G_F \times (\text{Area})} = \frac{\frac{1}{18}\sigma_u\epsilon_u btl}{G_F bt} = \frac{\epsilon_u\lambda}{18 s_E} \quad \ldots\ldots (16)$$

Such a ratio is higher than unity when

$$\frac{s_E}{\epsilon_u\lambda} \leq \frac{1}{18} \quad \ldots\ldots (17)$$

Eq. 17 represents a more strict condition for global structural brittleness compared with Eq. 15.

Three-Point Bending of Slabs

When the shear forces cannot be neglected (in sufficiently slender beams) and the Poisson ratio is negligible, Eq. 1 is replaced by (Biolzi, private communication, n.d.)

$$\tilde{\delta} = \tilde{P}\left(\frac{1}{4}\lambda^3 + \frac{3}{5}\lambda\right) \quad \ldots\ldots (18)$$

whereas Eq. 12 becomes

$$\tilde{\delta} \leq \left(\frac{\lambda^3}{6} + \frac{2}{5}\lambda\right) \quad \ldots\ldots (19)$$

Snap-back is then expected for

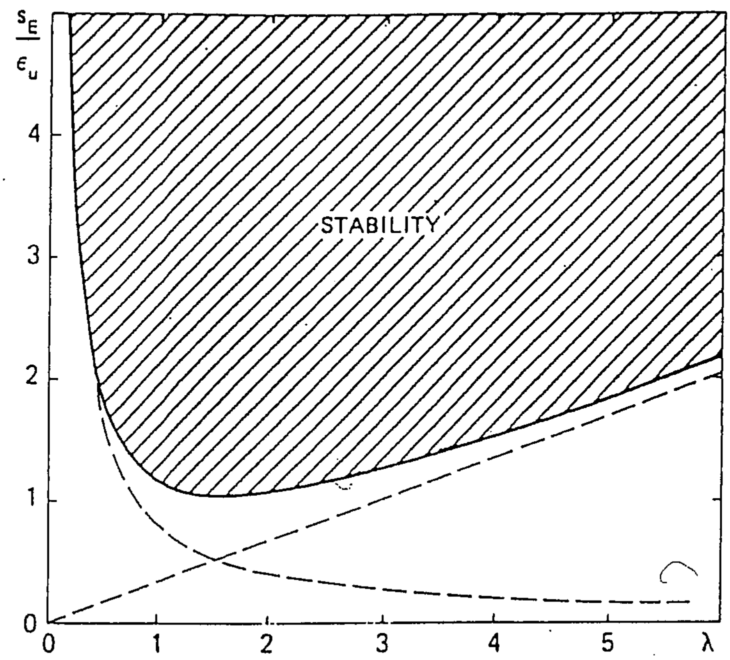

FIG. 3. Size-Scale versus Slenderness Locus of Snap-Back Instability

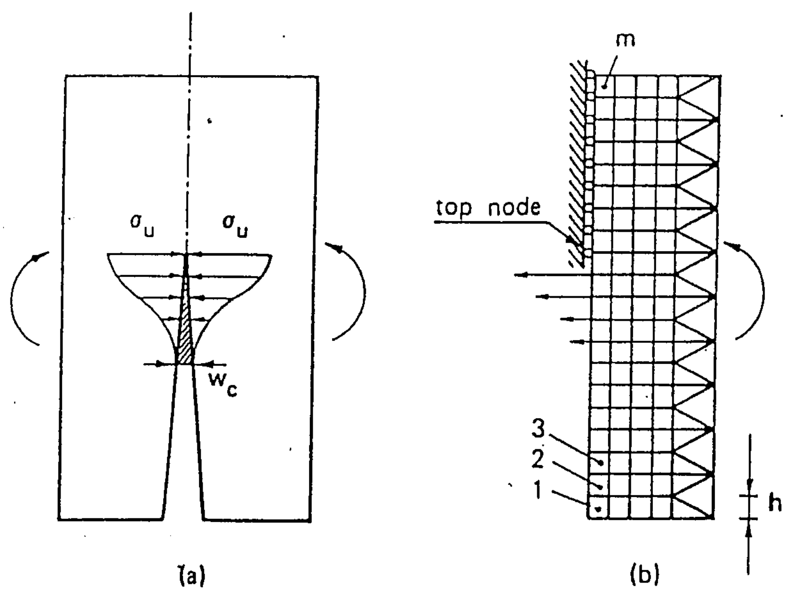

FIG. 4. Stress Distribution: (*a*) Across Cohesive Zone; (*b*) Equivalent Nodal Forces in Finite Element Mesh

$$\frac{s_E \lambda^2}{2\epsilon_u} \leq \left(\frac{\lambda^3}{6} + \frac{2}{5}\lambda\right) \qquad (20)$$

or

$$\frac{s_E}{\epsilon_u} \leq \left(\frac{\lambda}{3} + \frac{4}{5}\frac{1}{\lambda}\right) \qquad (21)$$

The system is brittle for low-brittleness numbers s_E and high ultimate strains ϵ_u, whereas low slendernesses λ ($\lambda \lesssim 1.55$) produce a clear trend toward unstable behavior (Fig. 3). Let us observe that below the ratio $s_E/\epsilon_u \simeq 1.03$, instability is always predicted.

Strain Localization and Apparent Strength of Initially Uncracked Slabs

The cohesive crack model is based on the following assumptions (Carpinteri 1985a; Hillerborg et al. 1976; Hillerborg 1985; Petersson 1981):

1. The cohesive fracture zone (plastic or process zone) begins to develop when the maximum principal stress achieves the ultimate tensile strength σ_u.
2. The material in the process zone is partially damaged but still able to transfer stress. Such a stress is dependent on the crack opening displacement w.

The real crack tip is defined as the point at which the distance between the crack surfaces is equal to the critical value of crack opening displacement w_c. At this point, the normal stress vanishes [Fig. 4(*a*)]. On the other hand, the fictitious crack tip is defined as the point at which the normal stress attains the maximum value σ_u, and the crack opening vanishes [Fig. 4(*a*)].

The closing stresses acting on the crack surfaces [Fig. 4(*a*)] can be replaced by nodal forces [Fig. 4(*b*)]. The intensity of these forces depends on the opening of the fictitious crack w, according to the $\sigma - w$ constitutive law of the material. When the tensile strength σ_u is achieved at the fictitious crack tip, the top node is opened and a cohesive force starts acting across the crack, while the fictitious crack tip moves to the next node.

With reference to the three-point bending test (TPBT) geometry shown in Fig. 5, the nodes are distributed along the potential fracture line. The coefficients of influence in terms of node openings and deflection are computed by a finite element analysis in which the fictitious structure shown in Fig. 5 is subjected to $(n + 1)$ different loading conditions. Consider the TPBT shown in Fig. 6(*a*) with an initial crack of length a_0 and the tip in node k. The crack opening displacements at the n fracture nodes may be expressed as follows:

$$\boldsymbol{w} = \mathbf{K}\mathbf{F} + \mathbf{C}P + \boldsymbol{\Gamma} \quad \ldots\ldots (22)$$

in which $\boldsymbol{w}$ = vector of the crack opening displacements; $\mathbf{K}$ = matrix of the coefficients of influence (nodal forces); $\mathbf{F}$ = vector of the nodal forces; $\mathbf{C}$ = vector of the coefficients of influence (external load); P = external load; and $\boldsymbol{\Gamma}$ = vector of the crack opening displacements due to the specimen weight.

On the other hand, the initial crack is stress-free, and therefore

$$F_i = 0, \qquad \text{for } i = 1, 2, \ldots, (k-1) \quad \ldots\ldots (23a)$$

while at the ligament there is no displacement discontinuity

$$w_i = 0, \qquad \text{for } i = k, (k+1), \ldots, n \quad \ldots\ldots (23b)$$

Eqs. 22 and 23 constitute a linear algebraical system of $2n$ equations and $2n$ unknowns, i.e., the elements of vectors $\boldsymbol{w}$ and $\mathbf{F}$. If load P and vector $\mathbf{F}$ are known, it is possible to compute the beam deflection δ as

$$\delta = \mathbf{C}^T\mathbf{F} + D_P P + D_\gamma \quad \ldots\ldots (24)$$

where D_P = the deflection for $P = 1$; and D_γ = the deflection due to the specimen weight.

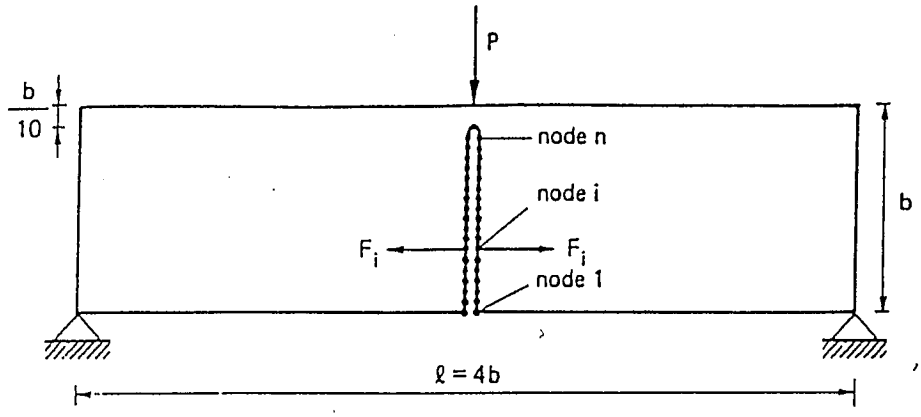

FIG. 5. Finite Element Nodes along Potential Fracture Line

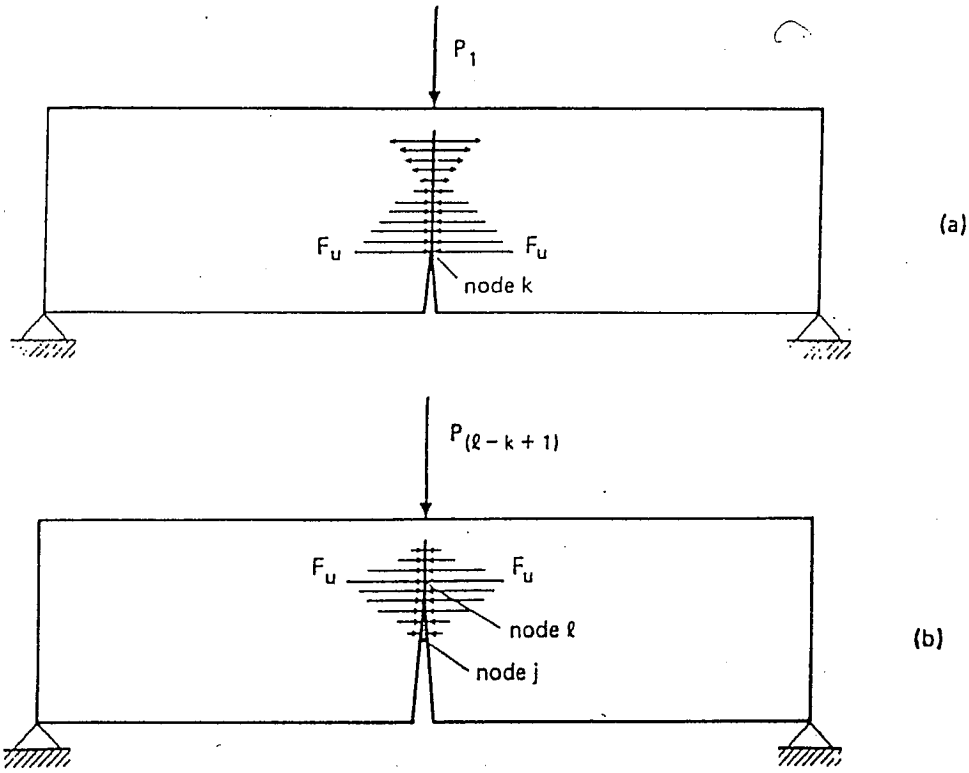

FIG. 6. Cohesive Crack Configurations at: (*a*) First Crack Growth Increment; (*b*) (1 − *k* + 1)th Crack Growth Increment

After the first step, a cohesive zone forms in front of the real crack tip [Fig. 6(*b*)], say between nodes j and l. Then Eqs. 23 are replaced by

$$F_i = 0, \qquad \text{for } i = 1, 2, \ldots, (j-1) \quad \ldots\ldots\ldots\ldots\ldots\ldots\ldots\ldots \quad (25a)$$

$$F_i - F_u\left(1 - \frac{w_i}{w_c}\right), \qquad \text{for } i = j, (j+1), \ldots, l \quad \ldots\ldots\ldots\ldots\ldots\ldots \quad (25b)$$

$$w_i = 0, \qquad \text{for } i = l, (l+1), \ldots, n \quad \ldots\ldots\ldots\ldots\ldots\ldots\ldots\ldots \quad (25c)$$

where F_u = the ultimate strength nodal force [Fig. 4(*b*)]

$$F_u = b\frac{\sigma_u}{m} \quad \ldots\ldots\ldots\ldots\ldots\ldots\ldots\ldots\ldots\ldots\ldots\ldots\ldots\ldots\ldots\ldots\ldots\ldots \quad (26)$$

Eqs. 22 and 25 constitute a linear algebraical system of $(2n + 1)$ equations

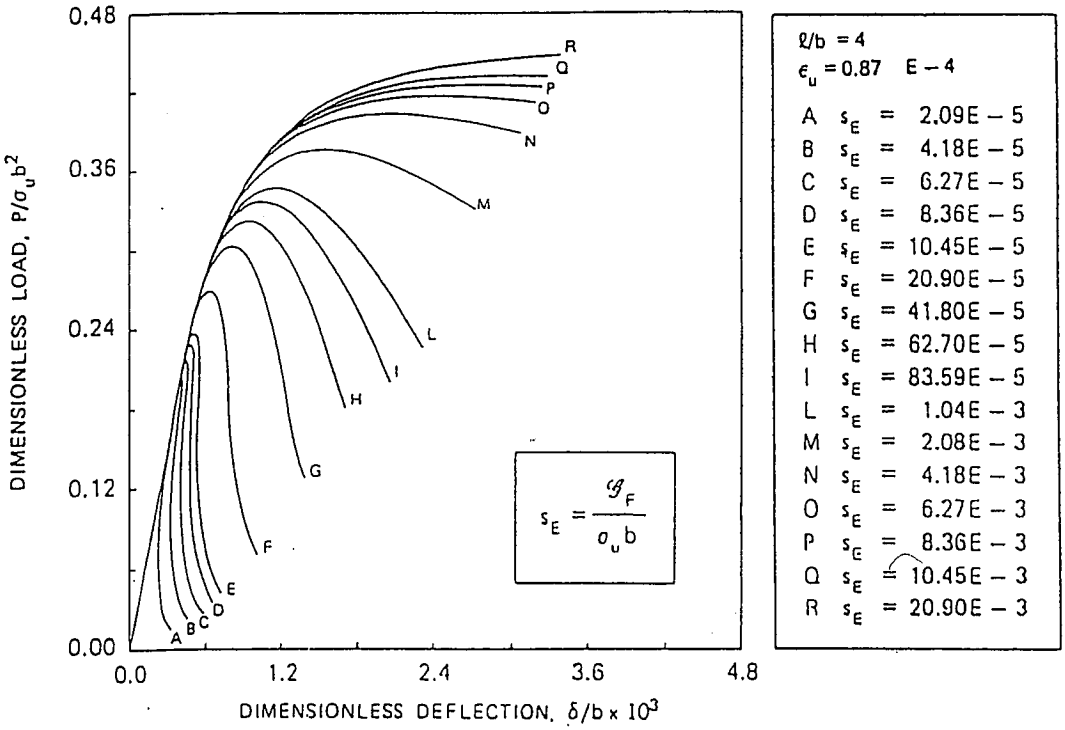

FIG. 7. Dimensionless Load versus Deflection Diagrams by Varying Brittleness Number [$s_E = G_F/\sigma_u b$ (λ = 4, a_0/b = 0.0, $\epsilon_u = 0.87 \times 10^{-4}$)]

and $(2n + 1)$ unknowns, i.e., the elements of vectors w and $\mathbf{F}$ and the external load P. At the first step, the cohesive zone is missing ($l = j = k$), and load P_1, which produces the ultimate strength nodal force F_u at the initial crack tip (node k), is computed. Such a value P_1, together with the related deflection δ_1 computed through Eq. 24, gives the first point of the P-δ curve. At the second step, the cohesive zone is between the nodes k and $(k + 1)$, and the load P_2, which produces the force F_u at the second fictitious crack tip (node $k + 1$) is computed. Eq. 24 then provides the deflection δ_2. At the third step, the fictitious crack tip is in the node $(k + 2)$, and so on. The present numerical program simulates a loading process in which the controlling parameter is the fictitious crack depth. On the other hand, real (or stress-free) crack depth, external load, and deflection are obtained at each step after an iterative procedure.

The program stops with the untying of node n and, consequently, with the determination of the last values F_n and δ_n. In this way, the complete load-deflection curve is automatically plotted by the computer.

Some dimensionless load-deflection diagrams for a concrete-like material are plotted in Fig. 7, with $a_o/b = 0.0$, $\epsilon_u = 0.87 \times 10^{-4}$, $\nu = 0.1$, $t = b$, $l = 4b$, and by varying the nondimensional number s_E. The specimen behavior is brittle (snap-back) for low s_E numbers, i.e., for low fracture toughnesses G_F, high tensile strengths σ_u, and/or large sizes b. For $s_E \leq 10.45 \times 10^{-5}$, the P-δ curve exhibits a positive slope in the softening branch and a catastrophic event occurs if the loading process is deflection-controlled. Such an unstable branch is not virtual only if the loading process is controlled by a monotonically increasing function of time (Fairhurst et al. 1971; Rokugo et al. 1986), e.g., the displacement discontinuity across the crack (Biolzi et al. 1987). On the other hand, Eq. 15 gives: $s_E \leq 11.60 \times 10^{-5}$. Such a condition reproduces that shown in Fig. 7 very accurately, whereas

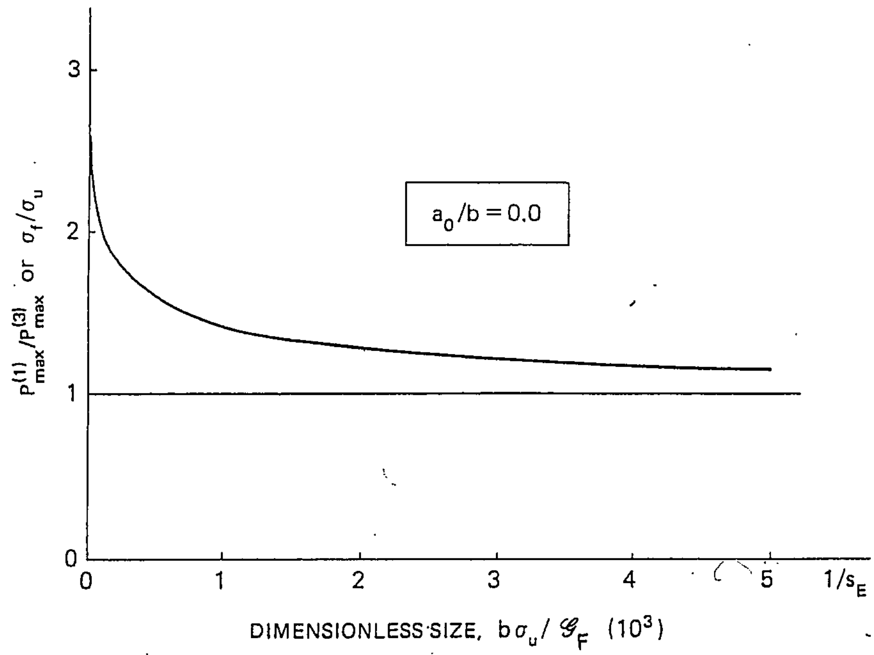

FIG. 8. Decrease in Apparent Strength by Increasing Specimen Size (λ = 4, a_0/b = 0.0, ϵ_u = 0.87 × 10^{-4})

Eq. 17 appears too severe. When the post-peak behavior is kept under control up to complete structural separation, the area delimited by the load-deflection curve and the deflection axis represents the product of fracture toughness G_F and the initial cross-section area, bt.

The maximum loading capacity $P^{(1)}_{max}$ of initially uncracked specimens with $l = 4b$ is obtained from Fig. 7. On the other hand, the maximum load $P^{(3)}_{max}$ of ultimate strength is given by

$$P^{(3)}_{max} = \frac{2}{3}\frac{\sigma_u t b^2}{l} \qquad (27)$$

The values of the ratio $P^{(1)}_{max}/P^{(3)}_{max}$ may also be regarded as the ratio of the apparent tensile strength σ_f (given by the maximum load $P^{(1)}_{max}$ and applying Eq. 27) to the true tensile strength σ_u (considered as a material constant). It is evident from Fig. 8 that the results of the cohesive crack model tend toward those of the ultimate strength analysis for low s_E values

$$\lim_{s_E \to 0} P^{(1)}_{max} = P^{(3)}_{max} \qquad (28)$$

Therefore, only for comparatively large specimen sizes can the tensile strength σ_u be obtained as $\sigma_u = \sigma_f$. With the usual laboratory specimens, an apparent strength higher than the true one is always found.

As a limit case, for the size $b \to 0$ or fracture energy $G_F \to \infty$ (elastic-perfectly plastic material in tension), i.e., for $s_E \to \infty$, the apparent strength $\sigma_f \to 3\sigma_u$. In fact, in the center of the beam, the uniform stress distribution (Fig. 9) produces a plastic hinge with a resistant moment M_{max} that is twice the classical moment of the birectangular limit stress distribution (elastic-perfectly plastic material in tension and compression).

The fictitious crack depth at the maximum load is plotted as a function of $1/s_E$ in Fig. 10. The brittleness increase for $s_E \to 0$ is also evident from this figure, in which the process zone at $dP/d\delta = 0$ tends to disappear (brit-

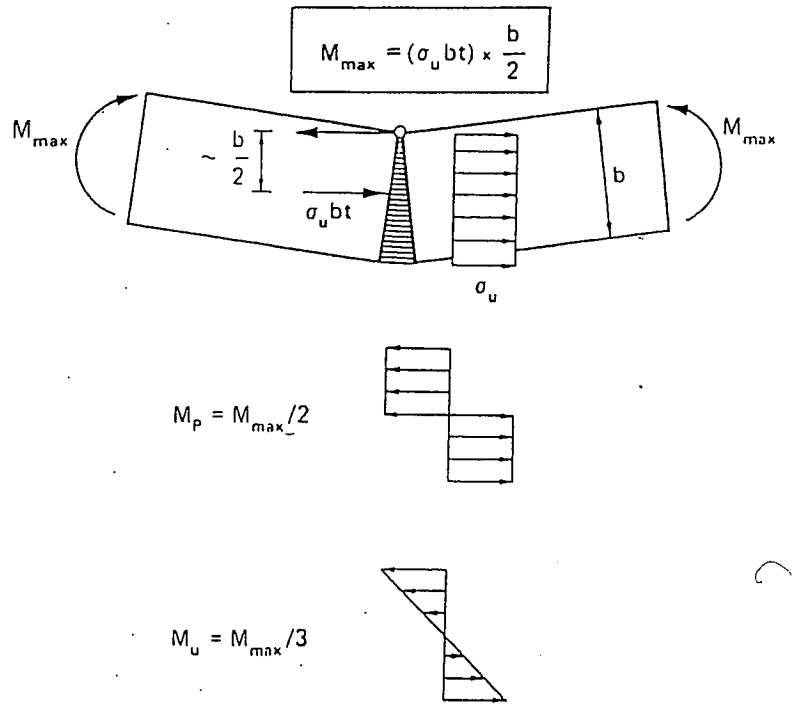

FIG. 9. Constant Distribution of Cohesive Stresses

tle collapse), whereas for $s_F \rightarrow \infty$ (ductile collapse), it tends to cover the whole ligament. On the other hand, the real (or stress-free) crack depth at the maximum load is always zero for each value of s_E. This means that the slow crack growth does not start before the softening stage. Therefore, neither the slow crack growth nor the cohesive zone develops before the peak, when $s_E \rightarrow 0$.

Referring again to Figs. 8 and 10, it is possible to state that the smaller the brittleness number s_E is, the more accurate the bifurcation is in reproducing the peprfectly brittle ultimate strength instability ($a_0/b = 0$).

The diagrams shown in Fig. 11 are related to higher beam slenderness, $\lambda = 16$. The same brittleness increase by decreasing s_E is obtained as previously discussed, but in this case, it is easier to achieve the snap-back instability of the beam, when $s_E \lesssim 62.70 \times 10^{-5}$. On the other hand, Eq. 15

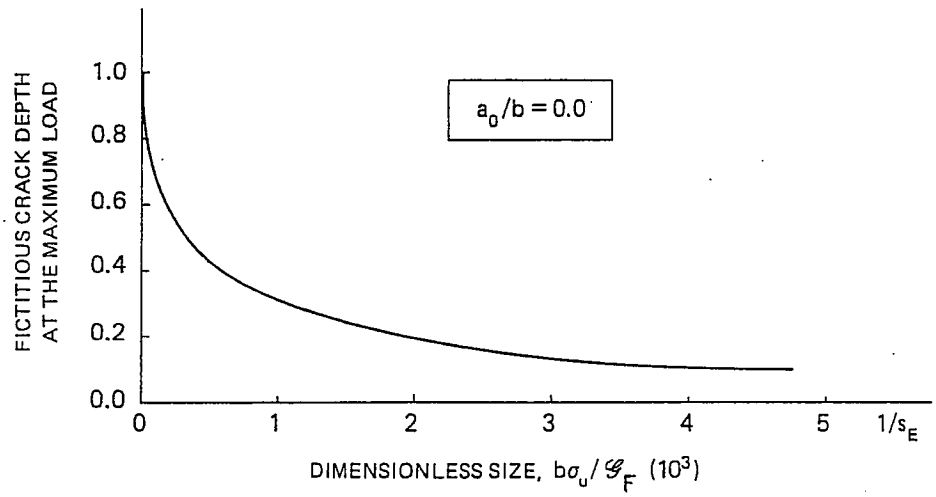

FIG. 10. Fictitious Crack Depth at Maximum Load as Function of Specimen Size ($\lambda = 4$, $a_0/b = 0.0$, $\epsilon_u = 0.87 \times 10^4$)

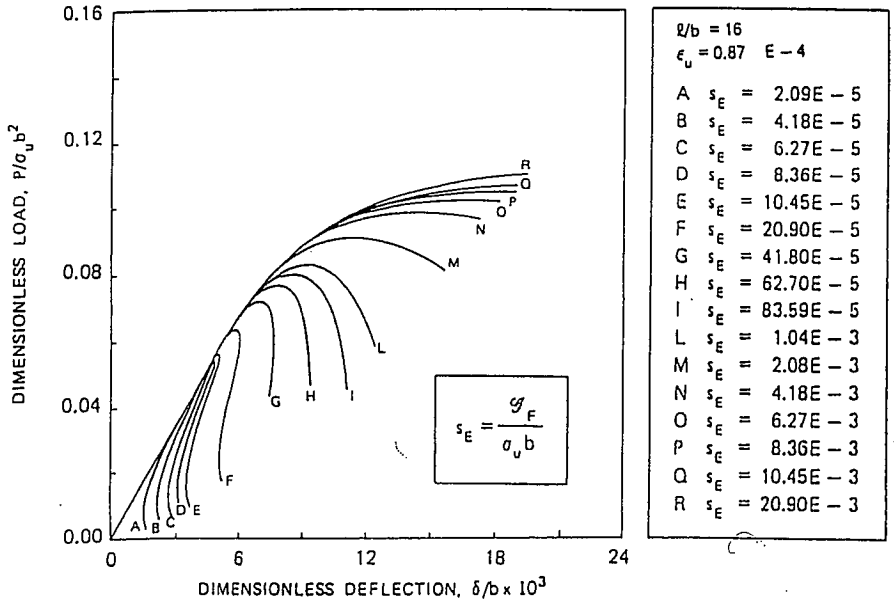

FIG. 11. Dimensionless Load versus Deflection Diagram by Varying Brittleness Number $S_E = G_F/\sigma_u b$ (λ = 16, a_0/b = 0.0, $\epsilon_u = 0.87 \times 10^{-4}$)

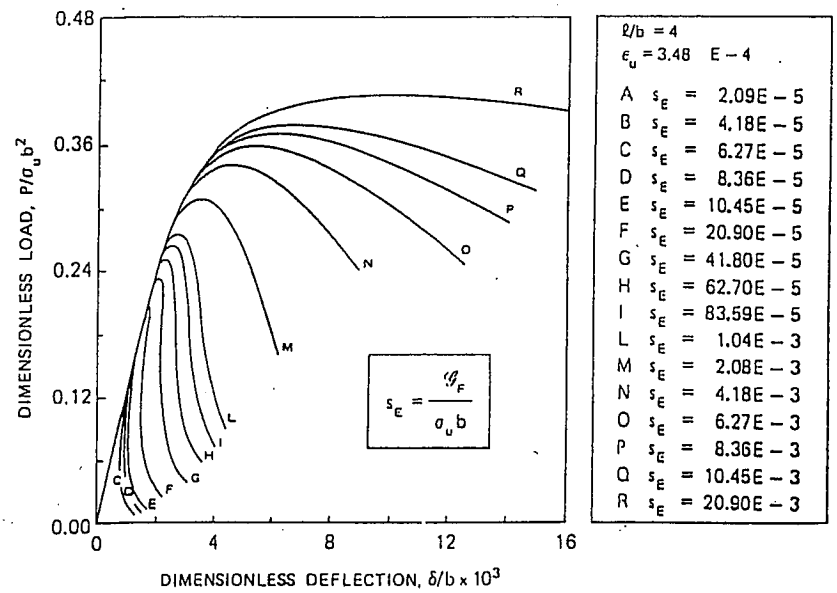

FIG. 12. Dimensionless Load versus Deflection Diagrams by Varying Brittleness Number $s_E = G_F/\sigma_u b$ (λ = 4, a_0/b = 0.0, $\epsilon_u = 3.48\ 10^{-4}$)

provides: $s_E \leq 46.40 \times 10^{-5}$, which is a good approximation.

The diagrams shown in Fig. 12 are related to higher ultimate strain which is four times the preceding one, $\epsilon_u = 3.48 \times 10^{-4}$ ($\lambda = 4$). Also in this case, the snap-back appears for $s_E \lesssim 62.70 \times 10^{-5}$. Obviously, Eq. 15 again provides $s_E \leq 46.40 \times 10^{-5}$, whereas Eq. 21 gives $s_E \leq 53.36 \times 10^{-5}$, which is a better approximation.

Cohesive Crack Propagation and Fictitious Fracture Toughness of Initially Cracked Slabs

The mechanical behavior of three-point bending slabs with initial cracks is investigated on the basis of the same cohesive numerical model presented

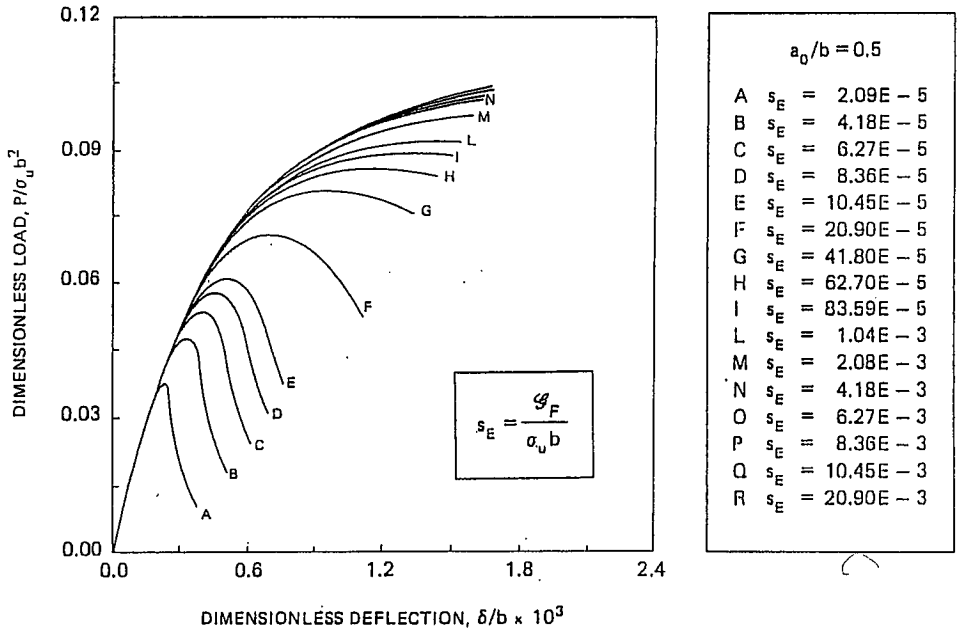

FIG. 13. Dimensionless Load versus Deflection Diagrams by Varying Brittleness Number $s_E = G_F/\sigma_u b$ ($\lambda = 4$, $a_0/b = 0.5$, $\epsilon_u = 0.87 \times 10^{-4}$)

in the preceding section. Some dimensionless load-deflection diagrams are shown in Fig. 13, for $a_0/b = 0.5$, $\epsilon_u = 0.87 \times 10^{-4}$, $\nu = 0.1$, $t = b$, $l = 4b$, and by varying the brittleness number s_E. The initial crack makes the specimen behavior more ductile than in the case of initially uncracked specimens. For the set of s_E numbers considered in Fig. 13, snap-back does not occur.

The area delimited by the load-deflection curve and the deflection axis represents the product of fracture toughness G_F times the initial ligament area, $(b - a_0)t$. The areas under the P-δ curves are thus proportional to the respective s_E numbers in Fig. 13 as well as in Figs. 7, 11, and 12. This simple result is due to the assumption that energy dissipation occurs only on the fracture surface, whereas in reality, energy is also dissipated in a damage volume around the crack tip, as assumed by Carpinteri and Sih (1984) and proved by Cedolin et al. (1987).

The maximum loading capacity $P^{(1)}_{\max}$, according to the cohesive crack model, is obtained as shown in Fig. 13. On the other hand, the maximum load $P^{(2)}_{\max}$ of brittle fracture can be obtained from the linear elastic fracture mechanics equation (ASTM, n.d.):

$$K_{IC} = \frac{P^{(2)}_{\max} l}{tb^{3/2}} f\left(\frac{a_0}{b}\right) \qquad (29a)$$

$$f\left(\frac{a_0}{b}\right) = 2.9\left(\frac{a_0}{b}\right)^{1/2} - 4.6\left(\frac{a_0}{b}\right)^{3/2} + 21.8\left(\frac{a_0}{b}\right)^{5/2} - 37.6\left(\frac{a_0}{b}\right)^{7/2} + 38.7\left(\frac{a_0}{b}\right)^{9/2} \qquad (29b)$$

in which $K_{IC} = \sqrt{G_F E}$ (plane stress condition).

The values of the ratio $P^{(1)}_{\max}/P^{(2)}_{\max}$ are reported as functions of the inverse of the brittleness number s_E in Fig. 14. Such a ratio may also be regarded

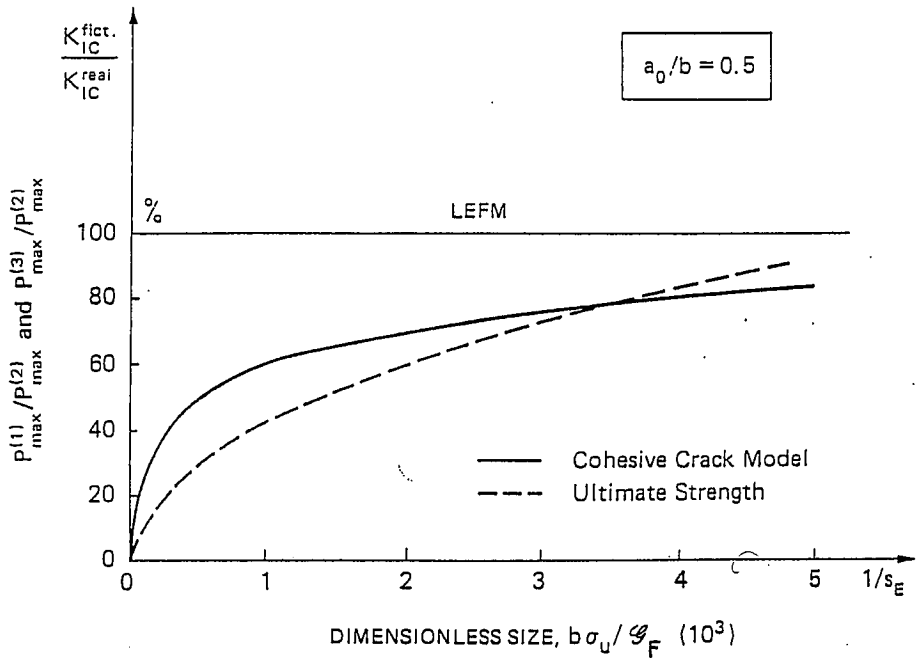

FIG. 14. Increase in Fictitious Fracture Toughness by Increasing Specimen Size ($\lambda = 4$, $a_0/b = 0.5$, $\epsilon_u = 0.87 \times 10^{-4}$)

as the ratio of the fictitious fracture toughness (given by the maximum load $P_{max}^{(1)}$) to the true fracture toughness (considered as a material constant).

It is evident that for low s_E numbers, the results of the cohesive crack model tend to those of linear elastic fracture mechanics:

$$\lim_{s_E \to 0} P_{max}^{(1)} = P_{max}^{(2)} \quad \ldots\ldots (30)$$

and therefore, the maximum loading capacity can be predicted by applying the simple condition $K_I = K_{IC}$. It appears that the true fracture toughness K_{IC} of the material can be obtained only with very large specimens. In fact, with the laboratory specimens, a fictitious fracture toughness lower than the true one is always measured (Barr and Bear 1977; Carpinteri 1981a, 1982b, 1985a; Ingraffea and Saouma 1985; Kasperkiewicz et al. 1986; Li et al. 1987; Li and Liang 1986; Shah 1984; Walsh 1972; Zaitsev and Kovler 1986; Ziegeldorf et al. 1980).

When the brittleness number $s_E \to 0$, $P_{max}^{(1)} \simeq P_{max}^{(2)}$, and Eq. 23 provides

$$G_F = P_{max}^2 \frac{\lambda^2 f^2\left(\frac{a_0}{b}\right)}{bt^2 E} \quad \ldots\ldots (31)$$

In a three-point bending specimen of linear elastic material, the deflection is given by the contribution of a distributed and a concentrated compliance, respectively:

$$\delta = \frac{P}{Et}\left[\frac{1}{4}\lambda^3 + \frac{3}{2}\lambda^2 g\left(\frac{a_0}{b}\right)\right] \quad \ldots\ldots (32)$$

where (Tada et al. 1963):

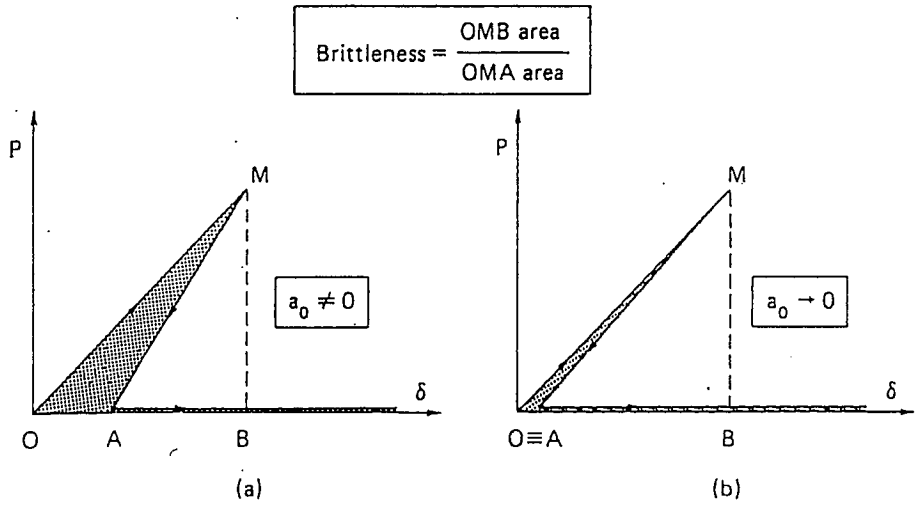

FIG. 15. Definition of Structure Brittleness as Ratio of Elastic Energy Contained in Body at Bifurcation Point to Energy Dissipated in Fracturing Process: (*a*) Initially Cracked Specimen of Infinite Size; (*b*) Uncracked Specimen of Infinite Size

$$g\left(\frac{a_0}{b}\right) = \left(\frac{\frac{a_0}{b}}{1-\frac{a_0}{b}}\right)^2 \left[5.58 - 19.57\left(\frac{a_0}{b}\right) + 36.82\left(\frac{a_0}{b}\right)^2 - 34.94\left(\frac{a_0}{b}\right)^3 + 12.77\left(\frac{a_0}{b}\right)^4\right] \quad \ldots\ldots (33)$$

Eq. 32 is also valid for the point of instability, and then Eq. 31 is transformed as follows:

$$G_F(b-a_0)t = \left(\frac{P_{\max}\delta_{\max}}{2}\right) \frac{2f^2\left(\frac{a_0}{b}\right)\left(1-\frac{a_0}{b}\right)}{\frac{1}{4}\lambda + \frac{3}{2}g\left(\frac{a_0}{b}\right)} \quad \ldots\ldots (34)$$

If brittleness is defined as the ratio of the elastic energy contained in the body at the point of instability to the energy that can be dissipated in the body [Fig. 15(*a*)], the result is a function of beam slenderness and initial crack depth:

$$\text{Brittleness} = \frac{\frac{1}{2}P_{\max}\delta_{\max}}{G_F(b-a_0)t} = \frac{\frac{1}{4}\lambda + \frac{3}{2}g\left(\frac{a_0}{b}\right)}{2\left(1-\frac{a_0}{b}\right)f^2\left(\frac{a_0}{b}\right)} \quad \ldots\ldots (35)$$

When the beam is initially uncracked, i.e., $a_0/b = 0$, the brittleness tends to infinity, and the softening branch is coincident with the elastic one [Fig. 15(*b*)]. On the other hand, when the initial crack length differs from zero ($a_0 \neq 0$), the brittleness tends to the value in Eq. 35 for the size-scale tending

to infinity [Fig. 15(*a*)]. In this case, the softening branch is always distinct from the elastic branch.

When the beam is initially uncracked, the elastic energy contained in the body at the point of instability is an infinite quantity of higher rank with respect to the fracture energy, the former being proportional to $b^3(\sigma_u^2/E)$ and the latter to b^2G_F. When there is an initial crack, the two quantities are of the same rank for the size-scale b tending to infinity, their ratio being finite and provided by Eq. 35.

Conclusions

1. Referring back to Figs. 8 and 14 it is possible to state that the smaller the brittleness number s_E, the more accurate the snap-back instability is in reproducing the perfectly brittle ultimate strength instability ($a_0 = 0$) or the linear elastic fracture mechanics instability ($a_0 \neq 0$).

2. Ultimate tensile strength σ_u or fracture toughness K_{IC} can be obtained exactly only with very large (initially uncracked or cracked, respectively) specimens (Bažant 1984; Carpinteri 1982b). On the other hand, the critical value G_F of strain energy release rate may be derived from the area delimited by the load-deflection curve and the deflection axis for any specimen size, when plastic (or volume) dissipation and distributed cracking are negligible.

3. The assumption of a linear σ-w diagram is only illustrative. On the other hand, it was shown by Carpinteri et al. (1987) that the present analysis is also applicable when the diagram is nonlinear.

Acknowledgments

The financial support of the Department of Public Education (M.P.I.) and of the National Research Council (C.N.R.) is gratefully acknowledged.

Appendix. References

ASTM. (1974). "Standard method of test for plane strain fracture toughness of metallic materials." *E 399-74*, ASTM.

Barr, B., and Bear, T. J. (1977). "Fracture toughness tests for concrete." *Int. J. Fracture*, 13, 92–96.

Bažant, Z. P. (1976). "Instability, ductility, and size effect in strain-softening concrete." *J. Engrg. Mech. Div.*, ASCE, 102(2), 331–344.

Bažant, Z. P. (1984). "Size effect in blunt fracture: concrete, rock, metal." *J. Engrg. Mech.*, ASCE, 110(4), 518–535.

Biolzi, L., et al. (1987). "Snap-back softening instability in high strength concrete beams." *Proc., SEM-RILEM Int. Conf. on Fracture of Concrete and Rock*, S. P. Shah and S. E. Swartz, eds.

Carpinteri, A. (1981a). "Size effect in fracture toughness testing: a dimensional analysis approach." *Proc. Int. Conf. on Analytical and Experimental Fracture Mechanics*, G. C. Sih and M. Mirabile, eds., Sijthoff and Noordhoff, 785–797.

Carpinteri, A. (1981b). "Static annd energetic fracture parameters for rocks and concretes." *Mater. Struct.*, RILEM, 14, 151–162.

Carpinteri, A. (1982a). "Application of fracture mechanics to concrete structures." *J. Struct. Div.*, ASCE, 108(4), 833–848.

Carpinteri, A. (1982b). "Notch sensitivity in fracture testing of aggregative materials." *Engrg. Fract. Mech.*, 16, 467–481.

Carpinteri, A. (1985a). "Interpretation of the Griffith instability as a bifurcation of the global equilibrium." *Proc., NATO Advanced Research Workshop on Appli-*

cation of Fracture Mechanics to Cementitious Composites, S. P. Shah, ed., Martinus Nijhoff, 287–316.
Carpinteri, A. (1985b). "Size effects on the brittleness of concrete structures." *A.I.T.E.C. Conf.*, 109–123 (in Italian).
Carpinteri, A. (1985c). "Softening instability and equilibrium branching in cohesive solids." *Proc., Euromech. Colloquium 198, Physical-Numerical Modelling in Nonlinear Fracture Mechanics*, J. H. Argyris, ed.
Carpinteri, A. (1986a). "A catastrophe theory approach to fracture mechanics." *Proc., Int. Conf. on Role of Fracture Mechanics in Modern Technology*, G. C. Sih, ed.
Carpinteri, A. (1986b). "Limit analysis for elastic-softening structures: scale and slenderness influence on global brittleness." *Brittle matrix composites 1*, A. M. Brandt and I. H. Marshall, eds., Elsevier Applied Science, 497–508.
Carpinteri, A. (1987). "Catastrophical softening behaviour and hyperstrength in low reinforced concrete beams." Presented at 25th CEB Plenary Session, Treviso, Italy, May 11–13.
Carpinteri, A., et al. (1987). "Numerical simulation of concrete fracture through a bilinear softening stress-crack opening displacement law." *Proc., SEM-RILEM Int. Conf. on Fracture of Concrete and Rock*, S. P. Shah and S. E. Swartz, eds., 178–191.
Carpinteri, A., Colombo, G., and Giuseppetti, G. (1986a). "Accuracy of the numerical description of cohesive crack propagation." *Fracture toughness and fracture energy of concrete*. F. H. Wittmann, ed., Elsevier, 189–195.
Carpinteri, A., Di Tommaso, A., and Fanelli, M. (1986b). "Influence of material parameters and geometry on cohesive crack propagation." *Fracture toughness and fracture energy of concrete*, F. H. Wittmann, ed., Elsevier, 117–135.
Carpinteri, A., et al. (1986c). "Experimental evaluation of concrete fracture energy through a new identification method." *Fracture toughness and fracture energy of concrete*, F. H. Wittmann, ed., Elsevier, 423–436.
Carpinteri, A., and Fanelli, M. (1987). "Numerical analysis of the catastrophical softening behaviour in brittle structures." *Proc., Fourth Int. Conf. on Numerical Methods in Fracture Mechanics*, Pineridge Press, 369–386.
Carpinteri, A., and Sih, G. C. (1984). "Damage accumulation and crack growth in bilinear materials with softening." *Theor. Appl. Frac. Mech.*, 1, 145–159.
Cedolin, L., Dei Poli, S., and Iori, I. (1987). "Tensile behaviour of concrete." *J. Engrg. Mech.*, ASCE, 113(3), 431–449.
Dougill, J. W. (1976). "On stable progressively fracturing solids." *Zeitschrift für Angewandte Mathematik und Physik (ZAMP)*, 27, 423–437.
Fairhurst, C., Hudson, J. A., and Brown, E. T. (1971). "Optimizing the control of rock failure in servo-controlled laboratory tests." *Rock Mech.*, 3, 217–224.
Hillerborg, A. (1985). "Results of three comparative test series for determining the fracture energy G_F of concrete." *Mater. Struct.*, RILEM, 18, 407–413.
Hillerborg, A., Modeer, M., and Petersson, P. E. (1976). Analysis of crack formation and crack growth in concrete by means of fracture mechanics and finite elements." *Cem. Concr. Res.*, 6, 773–782.
Ingraffea, A. R., and Gerstle, W. H. (1985). "Nonlinear fracture models for discrete crack propagation." *Proc., NATO Advanced Research Workshop on Application of Fracture Mechanics to Cementitious Composites*, S. P. Shah, ed., Martinus Nijhoff, 247–285.
Ingraffea, A. R., and Saouma, V. (1985). "Numerical modeling of discrete crack propagation in reinforced and plain concrete." *Fracture mechanics of concrete: Structural application and numerical calculation*, G. C. Sih and A. Di Tommaso, eds., Martinus Nijhoff Publishers, 171–225.
Jenq, Y. S., and Shah, S. P. (1985). "Two parameter fracture model for concrete." *J. Engrg. Mech.*, ASCE, 111(10), 1227–1241.
Kasperkiewicz, J., Dalhuisen, D., and Stroeven, P. (1986). "Structural effects in the fracture of concrete." *Brittle matrix composites 1*, A. M. Brandt and I. H. Marshall, eds., Elsevier Applied Science, 537–548.
Li, V. C., Chan, C. M., and Leung, K. Y. (1987). "Experimental determination of

the tension-softening relations for cementitious composites." *Cem. Concr. Res.*, 17, 441–452.
Li, V. C., and Liang, E. (1986). "Fracture processes in concrete and fiber-reinforced cementitious composites." *J. Engrg. Mech.*, ASCE, 112(6), 566–586.
Maier, G. (1968). "On the unstable behaviour in elastic-plastic beams in flexure." *Rendiconti, Classe de Scienze (A)*, Istituto Lombardo, Accademia di Scienze e Lettere, 102, 648–677 (in Italian).
Mazar, J., and Lemaitre, J. (1985). "Application of continuous damage mechanics to strain and fracture behaviour of concrete." *Proc., NATO Advanced Research Workshop on Application of Fracture Mechanics to Cementitious Composites*, S. P. Shah, ed., Martinus Nijhoff, 507–520.
Petersson, P. E. (1981). "Crack growth and development of fracture zones in plain concrete and similar materials." *Report TVBM 1006*, Lund Inst. of Tech., Lund, Sweden.
Roelfstra, P. E., and Wittmann, F. H. (1986). "Numerical method to link strain softening with failure of concrete." *Fracture toughness and fracture energy of concrete*, F. H. Wittmann, ed., Elsevier, 163–175.
Rokugo, K., Ohno, S., and Koyanagi, W. (1986). "Automatical measuring system of load-displacement curves including post-failure region of concrete specimens." *Fracture toughness and fracture energy of concrete*, F. H. Wittmann, ed., Elsevier, 403–411.
Rots, J. G., Hordijk, D. A., and de Borst, R. (1987). "Numerical simulation of concrete fracture in direct tension." *Proc., Fourth Int. Conf. on Numerical Methods in Fracture Mechanics*, Pineridge Press, 457–471.
Shah, S. P. (1984). "Dependence of concrete fracture toughness on specimen geometry and on composition." *Fracture mechanics of concrete: Material characterization and testing*, A. Carpinteri and A. R. Ingraffea, eds., Martinus Nijhoff Publishers, 111–135.
Tada, H., Paris, P., and Irwin, G. (1963). *The stress analysis of cracks handbook*. Del Research Corporation, St. Louis, Mo., 2.16–2.17.
Walsh, P. F. (1972). "Fracture of plain concrete." *Indian Concr. J.*, 44, 469–470, 476.
Zaitsev, Y. V., and Kovler, K. L. (1986). "Effect of specimen geometry, stress state and structure heterogeneity of cementitious composite materials on K_{IC}." *Brittle matrix composites 1*, A. M. Brandt and I. H. Marshall, eds., Elsevier Applied Science, 559–570.
Ziegeldorf, S., Müller, H. S., and Hilsdorf, H. K. (1980). "A model law for the notch sensitivity of brittle materials." *Cem. Concr. Res.*, 10, 589–599.